Nonlinear continuous-wave optical propagation in nematic liquid crystals: Interplay between reorientational and thermal effects

Alessandro Alberucci,[1,*] Urszula A. Laudyn,[2] Armando Piccardi,[3] Michał Kwasny,[2] Bartlomiej Klus,[2] Mirosław A. Karpierz,[2] and Gaetano Assanto[1,3,†]

[1]*Photonics Laboratory, Tampere University of Technology, FI-33101 Tampere, Finland*

[2]*Faculty of Physics, Warsaw University of Technology, PL-00662 Warsaw, Poland*

[3]*NooEL–Nonlinear Optics and OptoElectronics Lab, University "Roma Tre," I-00146 Rome, Italy*

(Received 2 March 2017; published 11 July 2017)

We investigate nonlinear optical propagation of continuous-wave (CW) beams in bulk nematic liquid crystals. We thoroughly analyze the competing roles of reorientational and thermal nonlinearity with reference to self-focusing/defocusing and, eventually, the formation of nonlinear diffraction-free wavepackets, the so-called spatial optical solitons. To this extent we refer to dye-doped nematic liquid crystals in planar cells excited by a single CW beam in the highly nonlocal limit. To adjust the relative weight between the two nonlinear responses, we employ two distinct wavelengths, inside and outside the absorption band of the dye, respectively. Different concentrations of the dye are considered in order to enhance the thermal effect. The theoretical analysis is complemented by numerical simulations in the highly nonlocal approximation based on a semi-analytic approach. Theoretical results are finally compared to experimental results in the Nematic Liquid Crystals (NLC) 4-trans-4'-n-hexylcyclohexylisothiocyanatobenzene (6CHBT) doped with Sudan Blue dye.

DOI: 10.1103/PhysRevE.96.012703

I. INTRODUCTION

Liquid crystals (LCs) are a fascinating state of matter, simultaneously exhibiting physical properties usually associated with either solids or liquids. This is due, with some exceptions [1], to the decoupling between positional and orientational order of the constituting organic molecules: Depending on the chemical structure and external physical conditions (temperature, pressure), molecular position and orientation are characterized by a different symmetry [2]. In this paper, we focus on the case in which the position of the molecules is random on the long range, whereas their direction shows a finite degree of orientational order, i.e., on the nematic phase.

Composition and arrangement of LCs reflect on their physical and optical properties: LCs usually behave as anisotropic crystals but with a pointwise direction of the principal axes [2]. At the same time, LCs show a high degree of tunability through the application of external fields [2]. Thermotropic LCs are also highly sensitive (including phase transitions) to temperature changes [3]. All these characteristics have been exploited for different applications in photonics [4–9]. LCs feature a very strong optical nonlinearity as well [10]. Depending on the excitation, different kinds of nonlinear mechanisms come into play, such as reorientational, thermal, photorefractive, electrostrictive, electronic responses, as well as due to modulation of the order parameter [11–15]. Hence, on the one hand, LCs are an ideal workbench to investigate the interplay between different nonlinearities [16–18], on the other hand nonlinear optics helps studying the properties of new LC mixtures, including those doped with dyes [19–21].

In the context of nonlinear optics, materials often exhibit an overall response resulting from the combination of various processes [22]. The interplay and competition of nonlinear mechanisms leads to a rich scenario of all-optical phenomena [23], in many cases adding extra degrees of tunability and disclosing new ways to optical manipulation and signal processing [17,24–32].

In this paper we address the interplay and competition of the two dominant LC nonlinearities when the input is a continuous wave (CW), that is, reorientational and thermo-optic responses to light, when the LC is in the nematic phase. We consider a standard planar cell much longer than the diffraction length of the input beam in order to study the mutual role of linear diffraction and nonlinear effects [33]. In fact, both nonlinearities manifest as pointwise changes in the refractive index. At the same time, both of them exhibit a highly nonlocal character, i.e., a light-induced perturbation much wider than the exciting beam [34–37]. Since reorientation usually dominates over thermo-optical effects in pure LCs, we consider a specific guest dopant added to the host LC mixture in order to enhance light absorption in a specific range of wavelengths [16,18]. Thereby, employing one wavelength inside and one outside the absorption band of the dye, we can evaluate the interaction of the two responses when simultaneously excited. Using the highly nonlocal approximation [34], we model the behavior of the two nonlinearities when acting alone or together, considering the propagation of a single beam. Finally, we compare our theoretical findings with experimental measurements.

II. NONLINEAR LIGHT PROPAGATION IN NEMATIC LIQUID CRYSTALS

In the nematic phase (nematic LCs, NLCs), the molecules lack positional order on the long range but have a high degree of orientational order on macroscopic distances [2]. NLCs are usually featured by a cylindrical symmetry around an axis, termed molecular director $\hat{n}$. Optically, $\hat{n}$ is the optic axis

*alessandro.alberucci@tut.fi

†assanto@uniroma3.it

of the effective uniaxial medium. To determine the values of each element of the dielectric tensor, the order parameter S is also required [2]. The two independent eigenvalues of the dielectric tensor are $n_\perp^2$ and $n_\parallel^2$, corresponding to plane waves propagating with phase velocities $c/n_\perp$ and $c/n_\parallel$, respectively (c is the speed of light in vacuum) and electric fields oscillating orthogonal or parallel to $\hat{n}$ for $n_\perp$ or $n_\parallel$, respectively. The strong thermo-optic effect in NLCs stems from the marked dependence of S on temperature [2], in turn yielding to the temperature dependence of the refractive indices $n_\perp$ and $n_\parallel$ [38],

$$n_\parallel(T) \approx A - BT + \frac{2(\Delta n)_0}{3}\left(1 - \frac{T}{T_{\rm NI}}\right)^\beta, \quad (1)$$

$$n_\perp(T) \approx A - BT - \frac{(\Delta n)_0}{3}\left(1 - \frac{T}{T_{\rm NI}}\right)^\beta, \quad (2)$$

where $T_{\rm NI}$ is the temperature of the nematic-isotropic transition for a given NLC mixture, whereas A, B, β, and $(\Delta n)_0$ are fitting parameters derived from experimental measurements [39]. From Eqs. (1) and (2) it is clear that $n_\perp$ increases with temperature if $n_\parallel > n_\perp$ [$(\Delta n)_0 > 0$ for positive NLCs], whereas $n_\parallel$ decreases at double rate with respect to $n_\perp$. Fundamental [40] and higher-order solitons [41] based on thermal nonlinearity have been reported in NLCs.

For a given direction of the wave vector $\boldsymbol{k}$, there are two eigensolutions of the Maxwell's equations, the ordinary and the extraordinary plane waves, respectively. The ordinary electric field (o-wave) is always orthogonal to the director $\hat{n}$ and the phase velocity of the wave is $c/n_o = c/n_\perp$. Conversely, the extraordinary (e-wave) electric field is coplanar with the wave vector $\boldsymbol{k}$ and the director $\hat{n}$, with a phase velocity $c/n_e = c/n_e(\theta)$ which depends on the orientation angle θ between $\boldsymbol{k}$ and $\hat{n}$ [38] ($n_e(0) = n_\perp$):

$$n_e(\theta) = \left(\frac{\cos^2\theta}{n_\perp^2} + \frac{\sin^2\theta}{n_\parallel^2}\right)^{-1/2}. \quad (3)$$

Moreover, the extraordinary beam propagates in the plane ($\boldsymbol{k}$,$\hat{n}$) with a Poynting vector tilted with respect to the wave vector by the walk-off angle $\delta = \arctan[\epsilon_a \sin 2\theta/(\epsilon_a + 2n_\perp^2 + \epsilon_a \cos 2\theta)]$ [42], where $\epsilon_a = n_\parallel^2 - n_\perp^2 > 0$ is the optical anisotropy, usually positive in NLCs. As already stated, the dominant nonlinear optical responses in NLCs excited by CW lasers are thermal and reorientational. Thermal nonlinear effects occur, for example, when absorption causes a reduction of the order parameter, with a net decrease (increase) of $n_\parallel$ ($n_\perp$) [33,43] [Eqs. (1) and (2)]. Instead, the reorientational nonlinearity originates from collective rotation of molecules induced by light [10,11,13]. In the case of reorientation, the electric field $\boldsymbol{E}$ of a light beam induces a molecular dipole which tends to align to $\boldsymbol{E}$. The net result is an electromagnetic torque $\boldsymbol{\Gamma} = \epsilon_0\epsilon_a(\hat{n}\cdot\boldsymbol{E})(\hat{n}\times\boldsymbol{E})$. The equilibrium position of the director is determined by the balance between the torque $\boldsymbol{\Gamma}$ and the elastic forces associated with intermolecular links and anchoring conditions [11]. When light is purely extraordinary polarized, the all-optical reorientation of the director $\hat{n}$ results in an increase of θ, leading in turn to an increase in $n_e(\theta)$, as stated by Eq. (3). The net effect is beam self-focusing. The reorientational nonlinearity is polarization dependent as well:

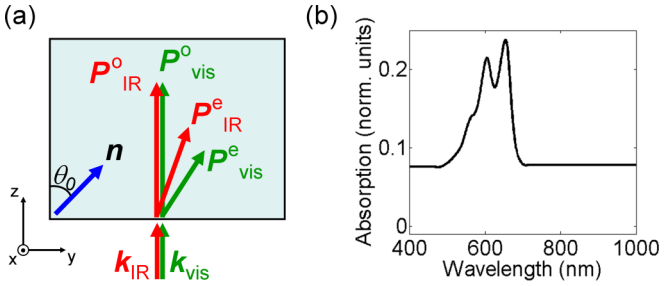

FIG. 1. (a) Sketch of the NLC sample. Two beams (subscripts IR and vis for $\lambda = 1064$ nm and $\lambda = 532$ nm, respectively) are launched collinearly. Inside the anisotropic NLC mixture the Poynting vector of the extraordinary components are still parallel while the energy propagates with different walk-off angles. (b) Absorption spectrum of the mixture of 6CHBT with 0.1% of Sudan Blue dye.

Ordinary input beams orientate the molecules only beyond the Fréedericksz threshold [44], whereas extraordinary beams can induce nonlinear effects at very low powers [45]. When an e-polarized bell-shaped beam propagates in NLCs, self-focusing at mW excitations can yield light self-confinement and the generation of bright spatial solitons, also termed nematicons [46]. Nematicons are self-trapped beams as well as light induced waveguides for copolarized signal(s) showing a high degree of tunability and reconfigurability [47–55]. An important feature of self-trapped beams in NLCs is the high degree of nonlocality characterizing the light-induced refractive index potential. As a matter of fact, the light-written index well extends far beyond the beam profile, thus preventing the insurgence of catastrophic collapse [35,56]. In this limit, the nonlinear index change Δn can be approximated by a parabolic shape $\Delta n = -\frac{\phi_2}{2}(x^2 + y^2)$, i.e., the system resembles a quantum harmonic oscillator [34]. In writing the expression for Δn, we assumed $\boldsymbol{k}\|\hat{z}$, with the plane xy normal to the wave vector. Nematicons are shape preserving, but in general spatial solitons in NLCs breathe with excitation dependent periodic oscillations in width and peak intensity [57]. The z dependence of the beam width for light propagating in a parabolic index well is given by [34,58,59]

$$\frac{n_0}{2}\frac{d^4w^2}{dz^4} + 2\phi_2\frac{d^2w^2}{dz^2} + 3\frac{d\phi_2}{dz}\frac{dw^2}{dz} + \frac{d^2\phi_2}{dz^2}w^2 = 0, \quad (4)$$

with n_0 the average refractive index and, in the nonlinear case, ϕ_2 depending on the light distribution.

III. SAMPLE GEOMETRY AND MATERIAL PROPERTIES

The sample is sketched in Fig. 1(a). To contain the NLC and maintain the desired molecular alignment, a planar cell was realized with two parallel glass slides separated by $L_x \approx 50$ μm, with the inner interfaces mechanically rubbed to yield uniform planar anchoring of the director at $\theta_0 = 45^\circ$ with respect to the z axis. The cell was filled with the host 4-trans-4'-n-hexylcyclohexylisothiocyanatobenzene (6CHBT) ($n_\perp = 1.5021$, $n_\parallel = 1.6314$ @$\lambda = 1064$ nm and $n_\perp = 1.52$, $n_\parallel = 1.6746$ @$\lambda = 532$ nm, room temperature) doped with 0.1% of the Sudan Blue dye [60], the latter showing a main absorption peak at $\lambda \approx 604$ nm [see Fig. 1(b)].

Light attenuation in an NLC sample can be described by the (intensity) absorption coefficient α_{ov}:

$$\alpha_{ov} = \alpha_{el} + \alpha. \tag{5}$$

According to Eq. (5), the power inside the NLC is $P = P_0 e^{-\alpha z}$, where P_0 is the input power in $z = 0$. The term α_{el} corresponds to the Rayleigh-like scattering, thus implying no changes in temperature. Conversely, the term α accounts for inelastic scattering, responsible for warming up the sample. When a resonant dye is added to the NLC host, in the limit of small concentrations only the term α changes, allowing us to control the amount of heat generated by light in the NLC. In addition, the strong NLC anisotropy yields, in general, a dichroic response, with α_{ov} depending on the polarization.

We used two CW laser beams of different wavelengths to change the relative weight of the two nonlinear responses. The beam at $\lambda = 1064$ nm is away from the dye resonance. The second beam, with wavelength $\lambda = 532$ nm, is within the absorption band of Sudan Blue to enhance the thermal nonlinearity [16]. The two beams are coupled into the sample by focusing them with a microscope objective to a waist of ≈ 3 μm at the input section $z = 0$. The beam evolution is observed by collecting the out-of-plane scattered light with a Charge-Coupled Device (CCD) camera connected to a commercial microscope.

IV. COMPARISON BETWEEN REORIENTATIONAL AND THERMAL NONLINEARITIES

A. Reorientational nonlinearity

The most known all-optical effect in NLC for CW excitations is the reorientational nonlinearity. Describing the director distribution by the angle θ, molecular reorientation in the single elastic constant approximation obeys [2]

$$\nabla^2\theta + \frac{\epsilon_0\epsilon_a(T)}{4K(T)}\sin[2(\theta - \delta(\theta,T))]|E|^2 = 0, \tag{6}$$

where E is the slowly varying envelope of the propagating field. In Eq. (6) we wrote explicitly the dependence of the material parameter (ϵ_a and the Frank's elastic constant K) on the temperature T. Eq. (6) is valid for a linear input polarization, with the field parallel to $\hat{x}$ (the ordinary component in the unperturbed NLC, with reorientation in the xz plane) or to $\hat{y}$ (extraordinary component, reorientation in yz). As is well known, the ordinary wave is subject to the optical Fréedericksz threshold, that is, the director starts to rotate only beyond a given optical power [13,33]; conversely, the extraordinary component undergoes threshold-less reorientation, allowing for the observation of self-focusing even at modest powers. In particular, for small reorientations ($\theta = \theta_0 + \psi$ and $\psi \ll \theta_0$) we can assume $\theta \approx \theta_0$ in the *sine* term in Eq. (6), the latter thus becoming a Poisson's equation, linear in beam intensity $I \propto |E|^2$. Hereafter we will proceed in the small reorientation approximation when solving Eq. (6), consistently with the configuration shown in Sec. III and described by $\theta_0 = \pi/4$ [42].

B. Thermal nonlinearity

Simultaneously to the torque exerted on the NLC molecules, the beam heats the sample through absorption. Neglecting convection [61], the temperature fulfills a Poisson's equation

$$\nabla^2 T = -\frac{\alpha^j n^j}{2\kappa Z_0}|E|^2 \quad (j = \text{ext, ord}), \tag{7}$$

where Z_0 is the vacuum impedance. In Eq. (7) both the optical absorption α^j and the refractive index n^j change according to the polarization [with ordinary index $n_\perp$ or extraordinary index given by Eq. (3)] of the propagating wave. In writing Eq. (7), we neglected the spatial anisotropy of the thermal conductivity κ in NLC [38].

C. Interplay between heat flow and molecular reorientation

Equations (6) and (7) allow us to compute the nonlinear perturbation of the temperature distribution and the director field. Once T and θ are known, Eqs. (1)–(3) allow us to describe the overall index well—$n_e(\theta,T)$ or $n_o(T)$ according to the input polarization—induced by light.

The relative weight of the two nonlinearities and their consequent interplay can be addressed assuming a Gaussian intensity profile $I = \frac{2P}{\pi w^2}\exp[-2(x^2+y^2)/w^2]$ and neglecting the derivative in the propagation direction in Eqs. (6) and (7): In this limit a closed-form solution can be found for the Poisson's equation. The maximum transverse reorientation θ_m and temperature T_m (on beam axis) in the highly nonlocal limit $w \ll L_x$ are then [62]

$$\theta_m(\theta_0,w,P,T_m) = \theta_0 + C_\theta(\theta_0,T_m)P \times \sum_{l=0}^{\infty}\frac{1}{2l+1}\text{erfc}\left[\frac{\pi(2l+1)w}{2\sqrt{2}L_x}\right], \tag{8}$$

$$T_m(T_0,w,P) = T_0 + C_T^j P\sum_{l=0}^{\infty}\frac{1}{2l+1}\text{erfc}\left[\frac{\pi(2l+1)w}{2\sqrt{2}L_x}\right], \tag{9}$$

where $C_\theta(\theta_0,T_m) = \frac{\epsilon_0\epsilon_a(T_m)Z_0\sin[2(\theta_0-\delta_0(T_m))]}{2\pi K(T_m)n_e(\theta_0,T_m)\cos^2\delta_0(T_m)}$, $C_T^j = \frac{\alpha^j}{\pi\kappa}$, T_0 is the room temperature, and P is the beam power. Noteworthy, neither θ_m nor T_m depend explicitly on the wavelength. We stress that if the boundary conditions applied to Eqs. (6) and (7) are the same [63], the spatial profile of the nonlinear perturbation is the same for both the nonlinear mechanisms. This is true when the glasses at the cell interfaces conduce heat much more than the liquid crystal (see Appendix A 4) and whenever the anisotropy in the elastic properties and in the thermal conductivity of the NLC is neglected. In other words, the ratio between reorientational and thermal contributions does not vary point by point, at least for small variations of T_m and θ_m across the sample. A key parameter is the magnitude of the parabolic index well ϕ_2, unambiguously determining the intensity distribution of a single beam in the highly nonlocal limit. A simple analytical relationship between ϕ_2 and the beam intensity peak can be easily found by a Taylor's expansion [57]. For the reorientational and the thermal cases we respectively find

$$\phi_{2,\theta}(\theta_0,w,P,T_m) = \frac{C_\theta(\theta_0,T_m)}{\eta}\frac{dn_e}{d\theta}\bigg|_{T_m,\theta_0}\frac{P}{w^2}, \quad (10)$$

$$\phi^j_{2,T}(\theta_0,w,P,T_m) = \frac{C^j_T}{\eta}\frac{dn^j}{dT}\bigg|_{T_m,\theta_0}\frac{P}{w^2}\ (j=\text{ext,ord}), \quad (11)$$

with η a fit coefficient (equal to 2) introduced to improve the matching between the Snyder-Mitchell model and exact solutions [64,65].

The two quantities $\phi_{2,\theta}$ and $\phi_{2,T}$ can be substituted into Eq. (4) to find how the beam radius varies along z. Assuming $\phi_2 = \Omega/w^2$ in agreement with Eqs. (10) and (11), the beam width evolves according to [59]

$$\frac{d^4w^2}{dz^4} + \frac{2\Omega}{n_0 w^2}\frac{d^2w^2}{dz^2} - \frac{2\Omega}{n_0 w^4}\left(\frac{dw^2}{dz}\right)^2 = 0. \quad (12)$$

Let us now discuss the character—focusing or defocusing—of the two nonlinearities with respect to the initial temperature T_0 of the NLC layer. The coefficient $\phi_{2,\theta}$ is always positive because reorientation increases the refractive index. Conversely, $\phi^j_{2,T}$ can be either positive or negative, in agreement with Eqs. (1) and (2). In particular, $\phi^{\text{ord}}_{2,T}$ is negative, whereas $\phi^{\text{ext}}_{2,T}$ changes its sign as the director orientation θ varies via the coefficient $dn^{\text{ext}}/dT = dn_e/dT$, with θ changing the relative weight of $n_\perp$ and $n_\parallel$ in determining $n_e(\theta)$ [see Eq. (3)] [38]. Since for small anisotropy ϵ_a we can write

$$n_e(\theta) \approx n_\perp + \frac{\epsilon_a}{2n_\perp}\sin^2\theta \approx n_\perp + (n_\parallel - n_\perp)\sin^2\theta, \quad (13)$$

Equations (1) and (2) yield

$$\frac{dn_e}{dT} \approx -B - \left[\frac{(\Delta n)_0\beta}{3T_{\text{NI}}}\left(1-\frac{T}{T_{\text{NI}}}\right)^{\beta-1}\right](2-3\cos^2\theta_0). \quad (14)$$

Equation (14) states that, in our configuration with $\theta_0 = \pi/4$, the thermo-optic response for the extraordinary component is defocusing when $B > 0$. When $B < 0$ the response is defocusing if $T > [1-(\frac{6T_{\text{NI}}|B|}{\beta(\Delta n)_0})^{1/(\beta-1)}]T_{\text{NI}}$ is satisfied. For example, at $\lambda = 1064$ nm in the mixture 6CHBT with $\theta_0 = \pi/4$, Eq. (14) is negative only for temperatures above 307 K. Finally, the magnitude of the nonlinear effects increases as the temperature approaches the transition temperature T_{NI} [38].

D. Ordinary polarization

The ordinary case is simpler than the extraordinary case: Below the Fréedericksz threshold, only the thermal nonlinearity is active, thus light undergoes self-focusing (defocusing) when $dn_\perp/dT > 0$ ($dn_\perp/dT < 0$) [15], with beam dynamics determined by Eqs. (9) and (11). Reorientation occurs above the threshold, so both the nonlinear mechanisms take place at the same time. A crucial issue is whether reorientation or nematic-isotropic transition takes place first. With respect to the reorientational nonlinearity, the Fréedericksz threshold is expected to be first order due to the finite size of the beam and the presence of self-focusing [66]. Nonetheless, our case is more complicated than Ref. [66] due to the simultaneous excitation of the ordinary and the extraordinary components above threshold, yielding a polarization precession on the scale of the birefringent length $\frac{\lambda}{(n_\parallel - n_\perp)} \approx 8\lambda$ [67]. The width of the Green function of the full 3D system is approximately given by L_x [42,58], and thus the elastic response is expected to smooth out these fast variations in the director distribution. At variance with Ref. [67], the threshold value should not significantly vary between the planar and the homeotropic case. Let us now assume that the 3D spatial profile of the beam undergoes negligible variations before the lowest threshold, i.e., that the thermal focusing is negligible. The power P_{th} corresponding to the Fréedericksz threshold is found from Eq. (8) by setting $\theta_0 = 0$. The optical threshold power P_{th} is then [68]

$$P_{\text{th}}(T_m) = \frac{\pi n_\perp(T_m)K(T_m)}{\epsilon_0\epsilon_a(T_m)Z_0} \times\left[\sum_{l=0}^{\infty}\frac{1}{2l+1}\text{erfc}\left(\frac{\pi(2l+1)w}{2\sqrt{2}L_x}\right)\right]^{-1}. \quad (15)$$

Similarly, starting from Eq. (9), the power P_{NI} required to reach the nematic-to-isotropic transition is

$$P_{\text{NI}} = \frac{\pi\kappa(T_{\text{NI}}-T_0)}{\alpha}\left[\sum_{l=0}^{\infty}\frac{1}{2l+1}\text{erfc}\left(\frac{\pi(2l+1)w}{2\sqrt{2}L_x}\right)\right]^{-1}. \quad (16)$$

As expected, the ratio $\Gamma = P_{\text{th}}/P_{\text{NI}}$, determining which phenomenon occurs first, does not depend on the beam width w but only on material parameters, the latter depending on wavelength and temperature. The logarithm of the ratio $P_{\text{th}}/P_{\text{NI}}$ is graphed in Fig. 2 versus sample temperature for three values of absorption. When Γ is lower than 1, the threshold is overcome before the transition to the isotropic phase. Conversely, when $\Gamma > 1$ the Fréedericksz transition is preceded (hence, washed out) by the phase transition from the nematic to the isotropic state.

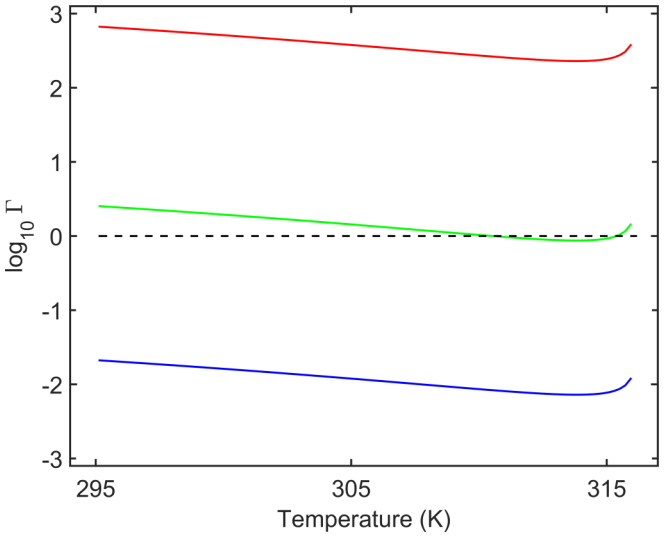

FIG. 2. Plot of $\log_{10}(\Gamma)$ versus temperature for $\alpha^{\text{ord}} = 10^2$, 8×10^2, and $9\times10^3\text{m}^{-1}$, from lower to upper curves, respectively. Here $\lambda = 532$ nm, $\kappa = 1.7\times10^{-1}$ Wm^{-1}K^{-1}, and $T_0 = 22\,^\circ$C.

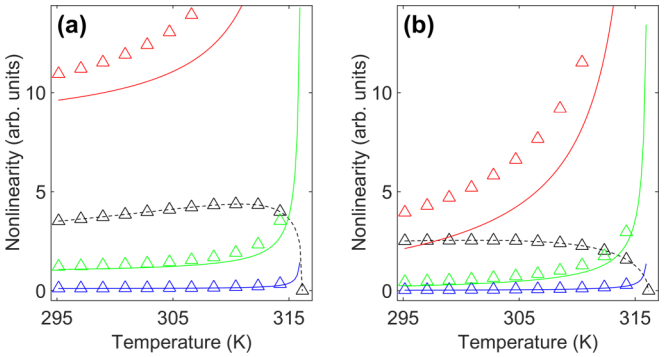

FIG. 3. Competition between reorientational and thermal nonlinearities for extraordinary waves in 6CHBT when (a) $\lambda = 532$ nm and (b) $\lambda = 1064$ nm, evaluated from Eq. (18) with $\theta_0 = \pi/4$. Dashed black line and solid lines are the left-hand side and the right-hand side of Eq. (18) versus sample temperature, respectively. The thermal nonlinearity is computed for $\alpha^{\rm ext} = 1 \times 10^2$ m^{-1} (bottom blue solid lines), 1×10^3 m^{-1} (middle green solid lines), and 9×10^3 m^{-1} (top red solid lines). Triangles correspond to the exact expressions, Eqs. (10) and (11).

E. Extraordinary polarization

The extraordinary polarization case is more complicated than the previous one due to direct competition of two nonlinearities with opposite signs [see Eq. (14)]. The overall nonlinear response will be focusing if $\phi_2 = \phi_{2,\theta} + \phi_{2,T} > 0$. Using Eqs. (10) and (11) we find

$$C_\theta(\theta_0, T_m)\frac{dn_e}{d\theta}\bigg|_{T_m,\theta_0} > -C_T\frac{dn_e}{dT}\bigg|_{T_m,\theta_0}. \tag{17}$$

Using Eqs. (13) and (14), conserving only the lowest-order terms in ϵ_a, Eq. (17) can be recast as

$$\frac{\epsilon_a^2(T_m)\sin^2(2\theta_0)}{16cn_\perp^2(T_m)K(T_m)} + \frac{\alpha^{\rm ext}(2-3\cos^2\theta_0)}{4\kappa}\frac{(\Delta n)_0\beta}{3T_{\rm NI}} \times\left(1-\frac{T_m}{T_{\rm NI}}\right)^{\beta-1} > \frac{\alpha^{\rm ext}B}{4\kappa}. \tag{18}$$

Typical results are illustrated in Fig. 3 for parameters corresponding to the mixture 6CHBT. The overall nonlinearity will be defocusing (i.e., thermal heating prevailing on molecular reorientation) in the presence of a large absorption. When the absorption reduces, reorientation becomes dominant. The relative weight of the two mechanisms depends on temperature: thermal effects undergo a steep increase close to $T_{\rm NI}$, and thus reorientation dominates over heating for temperatures far below the transition. The temperature interval where the torque prevails on heating gets wider as absorption diminishes becomes very narrow for undoped NLC ($\alpha_{\rm ov}^{\rm ext} \approx \alpha_{\rm el}^{\rm ext} \approx 10^2$ m^{-1}). Figure 3 also shows that reorientational effects are lower in the green than in the IR if the thermal absorption is supposed to be the same at the two wavelengths.

F. Scalar fundamental soliton in dye-doped 6CHBT

Let us now specialize our general considerations to the sample we used in experiments and detailed in Sec. III. For the sake of simplicity, we neglect NLC dichroism and take α independent from the wave polarization. Such a choice is due to the limited amount of experimental data about linear dichroism in 6CHBT within the visible spectrum. We note, however, that a different absorption between the two polarizations does not imply any quantitative change in our results but only a different scaling with power. Incidentally, due to the different observable effects associated with absorption and scattering losses, the interplay between reorientational and thermal nonlinearities could become a novel approach to measure optical absorption coefficients in NLCs. We can estimate a strong absorption $\alpha \gg \alpha_{\rm el}$, equal to about 9×10^3 m^{-1}, for $\lambda = 532$ nm due to the presence of the dopant. At $\lambda = 1064$ nm no resonance with the dye is excited (negligible α) and $\alpha_{\rm ov} \approx 10^2$ m^{-1}, as in standard NLC. Figure 4 graphs the width of the fundamental (single-humped) soliton versus input power of the beams at the two wavelengths. These solitary waves are scalar, i.e., they encompass only one polarization (ordinary or extraordinary) at a given wavelength. The soliton features have to account for both nonlinearities with a twofold interplay: on one side, a direct competition between the two nonlinear index wells, i.e., between the two all-optical wave-guiding effects quantified by Eqs. (10) and (11) and plotted in Fig. 3 for the extraordinary polarization; and, on the other side, an increase in temperature changes the material properties, including the elastic response (via the effective Frank's constant K) and the dielectric response according to Eqs. (1) and (2) (see Appendix A2 and Fig. 11 in the Appendix for more details) [69].

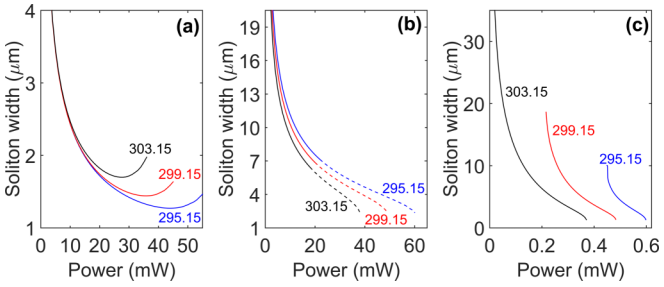

FIG. 4. Soliton width versus input power for infrared beam with extraordinary (a) and ordinary (b) polarization and ordinary green (c). We considered doped 6CHBT with $\theta_0 = \pi/4$ and absorption α of 10^2 m^{-1} (IR) and of 9×10^3 m^{-1} (green), respectively. The marked values are the initial temperatures T_0 in Kelvin. The dashed lines in the center panel correspond to overcoming the Fréedericksz threshold, inhibiting the observation of a purely thermal soliton.

The IR beam is able to excite a bright soliton with either input polarizations. When the polarization is extraordinary (y-polarized beam) reorientation overcomes thermal effects [see Fig. 3(b)]. An upper bound for soliton power exists due to the isotropic-to-nematic transition [see Eq. (16)]. The soliton width does not decrease monotonically with power, due to a decrease in the reorientational response via heating [see Fig. 3(b)]. The ordinary wave can also excite a soliton of purely thermal origin, even if such solitons are much wider than reorientational ones (tens of microns with respect to a few microns for typical powers, see Fig. 4). With reference to the reorientational soliton, the thermal effect increases as the transition to the isotropic phase is approached (Fig. 10). Noteworthy, to ensure the observability of a scalar thermal soliton, the power must remain below the Fréedericksz threshold, the

latter given by Eq. (15) once the waist of the corresponding soliton is used instead of the generic beam width w. In Fig. 4 (center panel) the existence branches where the Fréedericksz threshold is surpassed are marked by dashed lines.

Due to the much larger absorption and the different dispersion, self-trapping of green waves strongly differs from the infrared case. First, the extraordinary component never forms a bright soliton due to the dominant defocusing of thermal origin (Fig. 3). Conversely, an ordinary-wave thermal soliton can be formed. Due to the magnitude of the absorption, the soliton can be very narrow (see Fig. 12), the self-trapping can take place at very small powers (less than 1 mW) and in a very narrow range dependent on the initial temperature T_0. Similarly to the IR case, the power upper bound corresponds to the nematic-to-isotropic phase transition at $T > T_{\mathrm{NI}}$. The lower bound is associated with the peculiar dispersion of $n_\perp$ at this wavelength: For $T < 300.15$ K the ordinary index decreases with temperature (see Fig. 10 in the appendix), thus a bright soliton can exist only when the power inverts the sign of the nonlinearity and yields self-focusing. In agreement with this, the existence curves for solitons shift towards lower powers as the initial temperature increases.

V. EVOLUTION OF THE BEAM WIDTH

In this section, using Eqs. (4), (10), and (11), we use the semianalytical model of Ref. [70] to study theoretically how a fundamental Gaussian beam propagates in doped NLC, considering both polarizations separately and two wavelengths, one off-resonance (IR) and one (green) strongly absorbed. As input, we will take a Gaussian beam of input width w_0 and input power P_0 and possessing a flat phase profile in the input section $z = 0$.

A. IR beam alone

The behavior of the IR beam width versus z was computed numerically by solving Eq. (4) for different input powers and is plotted in Fig. 5. The behavior of the extraordinary component is shown in Figs. 5(a) and 5(b). In the calculation we included the thermal modulation of the NLC parameters (refractive indices and elastic constants) through absorption. In agreement with previous literature, strong self-focusing yields spatial solitons at a few mW powers. The dynamics of soliton formation depends on the input beam width: self-focusing of wider beams is eased due to less diffraction [70]. Losses due to Rayleigh scattering (not contributing to thermal heating) affect self-trapping and increase both the average beam width in propagation and the oscillation period (see solid and dashed lines in Fig. 5).

In the ordinary polarization, the beam follows a similar dynamics induced by the thermal nonlinearity, which is the only one active for powers below the Fréedericksz transition [expressed by Eq. (15)]. Even though the power required for self-focusing is much higher because of a lower nonlinearity, the influence of scattering losses and input beam width is analogous to the extraordinary case.

B. Green beam alone

The behavior of the green beam, when the input polarization is ordinary, is plotted in Fig. 6. At low powers, small increases

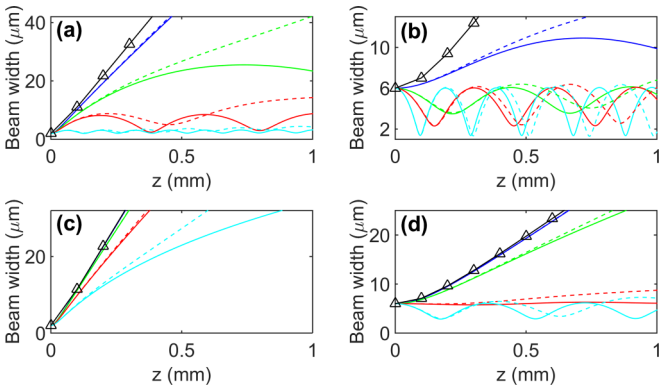

FIG. 5. Beam width versus z when $\lambda = 1064$ nm for $\alpha = 10^2$ m^{-1} and an input width $w_0 = 2$ μm [(a) and (c)] and $w_0 = 6$ μm [(b) and (d)], respectively. [(a) and (b)] Extraordinary wave subject to reorientational and thermal nonlinearity for input power $P_0 = 1$ mW (blue lines), 3 mW (green lines), 5 mW (red lines), and 10 mW (cyan lines). [(c) and (d)] Ordinary wave subject to a purely thermo-optic nonlinearity for input power $P_0 = 1$ mW (blue lines), 8 mW (green lines), 30 mW (red lines), and 50 mW (cyan lines). Solid and dashed lines correspond to zero Rayleigh scattering $\alpha_{\mathrm{el}} = 0$ and to $\alpha_{\mathrm{el}} = 4 \times 10^2$ m^{-1}, respectively. The black line with triangles plots the linear diffraction; the initial temperature T_0 is 295.15 K.

in beam divergence are observed due to the defocusing sign of $dn_\perp/dT$ for $T < 300.15$ K (see Fig. 10). At higher powers, the thermal nonlinearity becomes self-focusing. Due to the higher absorption α in the green, self-lensing is stronger near the input interface with respect to the infrared case, but self-trapping fades away more rapidly due to larger losses. In fact, as the absorption α increases (e.g., larger concentration of dopants), the minimum beam width gets smaller but, at the same time, the beam starts to freely diverge after shorter propagation distances z. This effect is prominent for small input beam widths [see Figs. 6(a) and 6(c)]. For wider input beams, self-trapping is more prone to occur and survives on larger distances from the input interface as well [Figs. 6(b) and 6(d)].

The propagation of the extraordinary green beam is more involved than in the infrared case: Due to the large absorption, thermal and reorientational nonlinearities are comparable, and both have to be accounted for simultaneously. The top row in Fig. 7 plots beam width versus z for an input width of 6 μm and four absorption coefficients α. For small absorption, reorientation is dominant and an overall focusing takes place. Between $\alpha = 2 \times 10^3$ m^{-1} and $\alpha = 3 \times 10^3$ m^{-1}, the thermal response overcomes the reorientational nonlinearity, yielding a monotonic increase in beam divergence versus input power as compared to the linear case, i.e., self-defocusing in agreement with Fig. 3. Due to the large increase in temperature, an extraordinary beam is also able to change its own trajectory: the light-induced temperature increments $T_m - T_0$ yield a power-dependent change in walk-off via Eqs. (1) and (2). In particular, for $\theta_0 = 45^\circ$ walk-off decreases with power due to the higher temperature: the wave-fronts remain unperturbed (the average wave vector remains normal to $\hat{z}$) but the Poynting vector changes direction. The bottom row of Fig. 7 shows the computed walk-off angle $\delta = \delta(\theta_0 = \pi/4, T = T_m)$ versus z. For $z \gg 1/\alpha_{\mathrm{ov}}$, the walk-off tends to $\delta = \delta(\theta_0 = \pi/4, T = T_0)$,

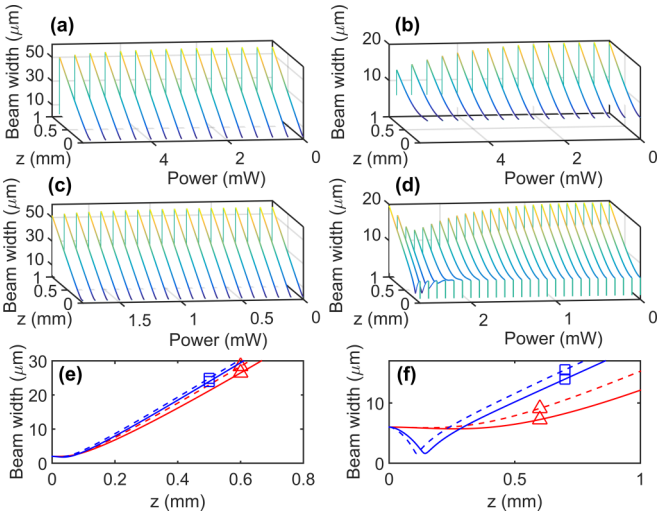

FIG. 6. Beam width versus z and input power when the input wave is purely ordinary at 532 nm and scattering losses are neglected. The thermal absorption α is 9×10^2 m^{-1} [(a) and (b)] and 3×10^3 m^{-1} [(c) and (d)], the input beam width w_0 is 2 μm [(a) and (c)] and 6 μm [(b) and (d)], respectively. Effects of scattering losses for $w_0 =$ 2 μm (e) and $w_0 = 6$ μm (f). Solid and dashed lines correspond to $\alpha_{\rm el} = 0$ and $\alpha_{\rm el} = 1 \times 10^3$ m^{-1}, respectively. Red (triangle) and blue (square) lines corresponds to $\alpha = 9 \times 10^2$ m^{-1} and $\alpha = 3 \times 10^3$ m^{-1}, respectively. Input powers are chosen at the edge of the isotropic-to-nematic transition. From (a)–(d) in (e) it is $P_0 = 5.8$ mW for $\alpha = 9 \times 10^2$ m^{-1} and $P_0 = 1.8$ mW for $\alpha = 3 \times 10^3$ m^{-1}. In (f) it is $P_0 = 5.8$ mW for $\alpha = 9 \times 10^2$ m^{-1} μm and $P_0 = 2.6$ mW for $\alpha = 3 \times 10^3$ m^{-1}. The initial temperature T_0 is 298.15 K.

i.e., the beam direction with respect to z corresponds to the linear case. Power-driven variations in walk-off mimic the trend of the maximum temperature T_m, with an exponential decay along z with slope given by the overall losses $\alpha_{\rm ov}$.

VI. COPROPAGATION OF A WEAK PROBE AND AN INTENSE IR BEAM

In this section we will investigate experimentally the light propagation when the impinging wavelength is outside the dye absorption band: We employed a diode-pumped solid state Nd:YAG laser emitting at $\lambda = 1064$ nm as an intense IR beam and frequency-doubled Nd:YAG laser operating at $\lambda = 532$ nm as a weak copropagating green beam. Both beams were coupled in the NLC cell after focusing with a microscope objective to a waist of about 3 μm. The width of both beams before the microscope objective was chosen to provide the same waist after focusing with a microscope objective. The beam evolution in the yz plane was analyzed by collecting the out-of-plane scattered light. To this extent, we used an optical microscope and a CCD camera, inserting a proper filter to let only the IR or green light through, whenever required. We launched a linear polarization exciting either ordinary (x-polarized) or extraordinary (y-polarized) waves.

Figure 8 illustrates the propagation of a weak probe (green) beam at $P_{vis} = 100$ μW, unable to excite either the reorientational nonlinearity or appreciable thermal effects, co-polarized and co-launched with an intense IR beam. The IR beam impinges normally to the sample, both for extraordinary and ordinary polarizations; the probe is launched so that its path in the NLC overlaps with the IR. Thus, the green beam wave vector in the extraordinary polarization is tilted so that the two waves share the same Poynting vector direction, regardless of dispersion and walk-off (Fig. 10).

Let us start with the ordinary polarization. The beam evolution for various IR beam powers is plotted in Figs. 8(a)–8(d). Figure 8(e) shows the normalized beam width w/w_0 and the beam shift Δy with respect to the input section versus the input IR power, measured at a distance $z = z_p = 0.25$ mm from the input interface. No appreciable variations are observed, neither in beam size nor in trajectory. Regarding the latter, no changes are expected as the walk-off is zero for this polarization. With reference to the beam size, Fig. 4 predicts a minimum soliton width of about 7 μm around $P = 20$ mW; due to the fact that the input waist is about 3 μm, the ordinary wave is negligibly affected by thermal self-focusing. Such behavior is also confirmed by the calculated width in Fig. 5(c) in the presence of scattering losses (dashed lines), where even for $P = 50$ mW the beam undergoes spreading at $z_p = 0.25$ mm. Furthermore, the Fréedericksz transition, estimated at powers just below 20 mW (Fig. 4), is not observed up to $P_{IR} = 50$ mW, when detrimental effects from heating (like formation of isotropic

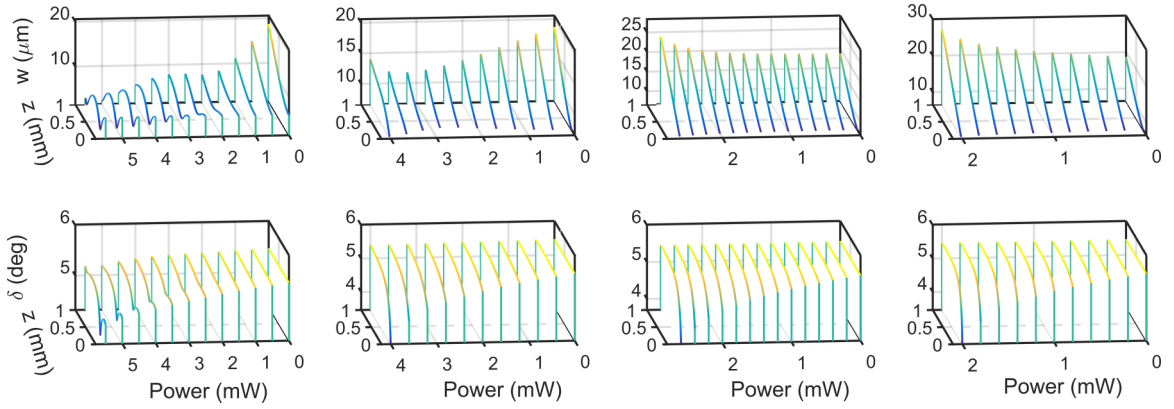

FIG. 7. Beam width w (top row) and walk-off angle δ (bottom row) versus z and the input power P_0 when the input polarization is extraordinary at 532 nm. Thermal absorption α is 1×10^3 m^{-1}, 2×10^3 m^{-1}, 3×10^3 m^{-1}, and 4×10^3 m^{-1} from left to right, respectively. T_0 is 298.15 K and w_0 is 6 μm.

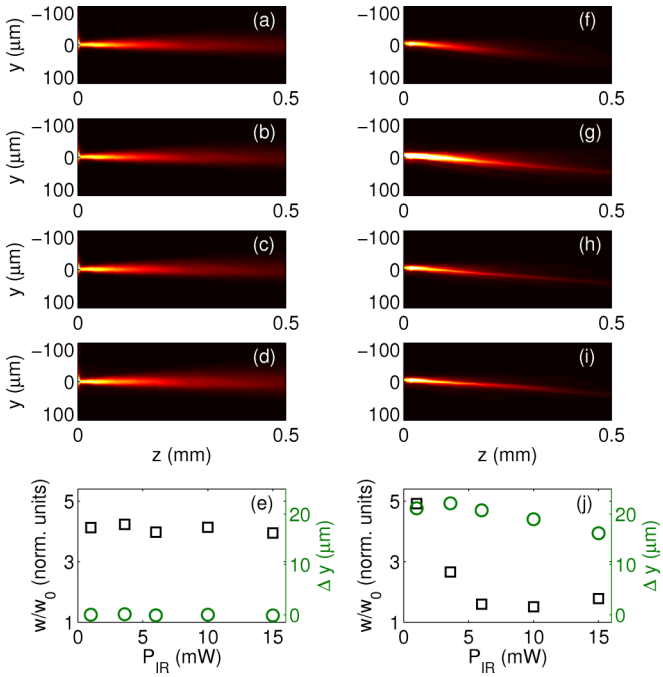

FIG. 8. Experimentally acquired photographs of a green probe beam copolarized and copropagating with an IR beam in the yz observation plane of a planar cell. When the two beams are ordinary waves [(a)–(d)], the Fréedericksz transition inhibits changes in either width [normalized to the initial value $w_0 = w(z = 0)$] and Poynting vector; the IR power is (a) $P = 1$ mW, (b) 3 mW, (c) 6 mW, and (d) 10 mW. Panel (e) summarizes normalized beam width and transverse displacement [$\Delta y \equiv y(z = z_p) - y(z = 0)$] due to walk-off in $z = z_p = 250$ μm. If the beams are extraordinary waves [see panels (f)–(i)], reorientation causes self-focusing and a nematicon guides the probe when (f) $P = 1$ mW, 3 mW (g), 6 mW (h), and 10 mW (i). (j) Same as in (e) but for extraordinary waves. The lower limit for the accuracy is about 1 μm and 0.2 for the position and the normalized width, respectively.

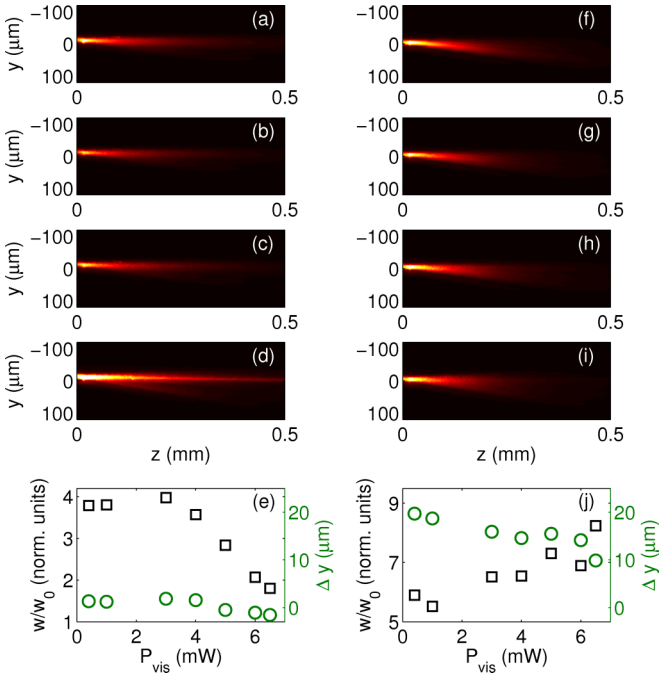

FIG. 9. Experimentally acquired photographs of the propagating visible beam (no IR). Ordinary wave propagation for $P = 0.4$ mW (a), 3 mW (b), 4 mW (c), and 6 mW (d), respectively, showing thermal self-focusing. (e) Normalized beam width w/w_0 and beam displacement Δy versus input power P. Propagation of extraordinary wave beam for $P = 0.4$ mW (f), 3 mW (g), 4 mW (h), and 6 mW (i), respectively: The extraordinary undergoes self-defocusing and power-dependent changes in trajectories. (j) Normalized width w/w_0 and transverse displacement Δy of the extraordinary beam versus input power. The lower limit for the accuracy is about 1 μm and 0.2 for the position and the normalized width, respectively.

bubbles related to the isotropic-nematic transition in NLC regions) take place. Aside from the approximations pointed out in the Sec. IV D, such discrepancy between theory and experiments can be attributed to inhomogeneities in director distribution at the cell entrance, possibly through the formation of a meniscus at the interface air-NLC. Such imperfections can affect reorientation more than the thermal flow.

The evolution of the extraordinary wave is shown in Figs. 8(f)–8(i) at four powers. For the sake of a quantitative discussion, Fig. 8(j) graphs the normalized beam width w/w_0 and lateral shift Δy in $z = z_p$. The extraordinary polarized beam at low powers has its Poynting vector at a walk-off angle $\delta(\pi/4) \approx 4.5^\circ$ (the theory predicts 4.8° at $T = 295$ K). Small variations can be observed in the beam trajectories with increasing powers, as lower walk-off is associated to a slightly reduced anisotropy in regions with higher temperatures (see Fig. 10). The width of the probe versus z shows appreciable changes for $P_{\rm IR} > 1$ mW due to the waveguide induced by molecular reorientation. The beam width at $z = z_p = 0.25$ mm is about the same as at the input section when $P_{\rm IR} \approx 4$ mW. This is in good agreement with Fig. 5(a), where the beam width reacquires the same value inside the NLC cell for powers between 3 and 5 mW. For higher powers, consistently with Fig. 5(a) the width measured in z_p oscillates around the size of a shape-preserving soliton, between 1.5 μm and 4 μm for 5 mW $< P <$ 40 mW according to the leftmost panel in Fig. 4.

VII. LIGHT PROPAGATION AT WAVELENGTH WITHIN THE ABSORPTION BAND OF THE DYE

When the green probe propagates by itself in the cell, the observed behavior drastically changes, as predicted. Let us first analyze the evolution of the ordinary component, shown in Figs. 9(a)–9(d) with quantitative features in Fig. 9(e). When the green power is above 3 mW, the beam experiences thermal self-focusing; for $P = 6.5$ mW, the beam shrinks down to a size close to the initial value; further increases in power eventually lead to the nematic-isotropic transition. This agrees well with the theoretical results plotted in Fig. 6. Finally, the transverse position of the ordinary beam slightly depends on the input power, due to slight variations in wave vector near the NLC-air interface and probably to a meniscus (as speculated in the previous case above), with slightly asymmetric boundary conditions near the beam entrance.

Considering the extraordinary polarization, graphed in Figs. 9(f)–9(j), a quasilinear increase of beam width versus

input power is observed [see Fig. 9(j)], associated with defocusing for $P > 1$ mW. The lateral displacement Δy at $P = 6.5$ mW is twice smaller than in the linear regime (low powers). According to the results reported in Fig. 7, such a deflection cannot be ascribed solely to thermally induced changes in walk-off. These experimental results prove that the wave vector undergoes a nonlinear deflection as well, analogously with what we previously described for green ordinary waves.

VIII. CONCLUSIONS

We investigated the interplay between two competing optical nonlinearities in NLCs, the reorientational and the thermal one. In the highly nonlocal limit and for small light-induced rotations of the director, the two effects share the same profile for the nonlinear perturbation. As a direct consequence, in the highly nonlocal regime the relative weight of the two responses does not depend on the the spatial profile of the input beam and it is spatially uniform across the NLC layer. We discussed theoretically the interplay between the two nonlinearities and its dependence on initial temperature and material absorption considering a monochromatic excitation. In particular, using the Green's function formalism, we computed for both the nonlinearities the effective nonlocal Kerr coefficients [42], the latter providing the width of the corresponding shape-preserving soliton. Using the Ehrenfest's theorem applied to the first- and second-momentum of the beam [59], we then generalized our results to the case of z-variant nonlinear waves (i.e., breather solitons).

We demonstrated that there are two different aspects to account for: (i) a direct competition on forming the overall nonlinear index well and (ii) a modulation of the parameters determining the NLC response to light. We showed that mechanism (i) plays a relevant role only in doped NLCs or in undoped NLCs very close to the isotropic-nematic transition. With reference to the case (ii), light-induced changes in temperature significantly affect the formation of reorientational solitons even in the undoped case, including the existence of solitons in a limited power range and a nonmonotonic soliton width versus power. The qualitative behavior has been experimentally confirmed investigating both ordinary and extraordinary propagation in a doped NLC (6CHBT plus Sudan Blue dye) with two different beams at 1064 nm (non-resonant with the dye) and at 532 nm (resonant with the dye).

Our findings widen the perspective on the unique optical properties of NLCs, the latter being an ideal workbench for the study of nonlinear optics and the interaction between nonlinearities [23,71]. Future developments include the simultaneous propagation of two beams at different wavelengths and with different profiles [18]. Generalizations to nonlinearities acting on distinct time scales can be envisaged as well when using pulsed sources [17]. Our results, together with semianalytic models accounting for self-lensing and its dynamics in propagation, show how nonlinear optics in long samples is an important tool for the complete characterization of NLC mixtures.

ACKNOWLEDGMENTS

A.A. and G.A. thank the Academy of Finland for support through the Finland Distinguished Professor Grant No. 282858. Funding from the National Science Centre of Poland under Grant No. DEC-2012/06/M/ST2/00479 is gratefully acknowledged.

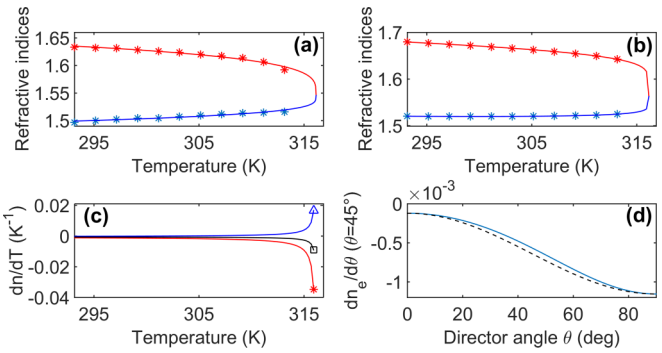

FIG. 10. Refractive indices $n_\parallel$ (red lines, upper curves) and $n_\perp$ (blue lines, bottom curves) versus temperature for (a) $\lambda = 1064$ nm and (b) $\lambda = 532$ nm; solid lines and symbols are fits and measurements, respectively. (c) Derivatives with respect to temperature of $n_\parallel$ (red line with star), $n_\perp$ (blue line with triangle), and $n_e(\theta = \pi/4)$ (black line with square) as computed from Eq. (14) at $\lambda = 532$ nm. (d) Derivative of n_e with respect to the director angle θ versus θ for $\lambda = 532$ nm and $T = 293$ K. Blue solid and black dashed lines are the exact expression (A1) and the corresponding approximation (14), respectively.

APPENDIX

1. Linear optical parameters of the mixture 6CHBT

Figures 10(a) and 10(b) shows the comparison between actual measurements carried out with an Abbe refractometer and fitting curves given by Eqs. (1) and (2) for the two wavelengths we used in this work. A best-fit procedure provides $A = 1.5295$, $B = -5.1364 \times 10^{-5}$, $(\Delta n)_0 = 0.2767$, and $\beta = 0.2719$ for $\lambda = 1064$ nm, whereas we find $A = 1.7098$, $B = 4.6545 \times 10^{-4}$, $(\Delta n)_0 = 0.2345$, and $\beta = 0.1483$ for $\lambda = 532$ nm. Having ascertained the quality of the fitting curves, the latter can be used to compute the derivative of $n_\parallel$ and $n_\perp$ with respect to temperature, as shown in Fig. 10(c). Finally, Fig. 10 provides a direct comparison between the approximated formula (14) and the exact expression

$$\frac{dn_e}{dT} = \left(\frac{\cos^2\theta}{n_\perp^2} + \frac{\sin^2\theta}{n_\parallel^2}\right)^{-\frac{3}{2}} \left[\frac{\cos^2\theta}{n_\perp^3}\frac{dn_\perp}{dT} + \frac{\sin^2\theta}{n_\parallel^3}\frac{dn_\parallel}{dT}\right]. \tag{A1}$$

2. Elastic properties of the mixture 6CHBT

When anisotropy of the elastic properties of the NLC is accounted for, the reorientation induced by an optical wavepacket invariant along z is given by

$$(K_1\cos^2\theta + K_3\sin^2\theta)\frac{\partial^2\theta}{\partial y^2} + K_2\frac{\partial^2\theta}{\partial x^2} + (K_3 - K_1)\sin(2\theta)\left(\frac{\partial\theta}{\partial y}\right)^2 + \frac{\epsilon_0\epsilon_a}{4}\sin[2(\theta-\delta)]|E|^2 = 0. \tag{A2}$$

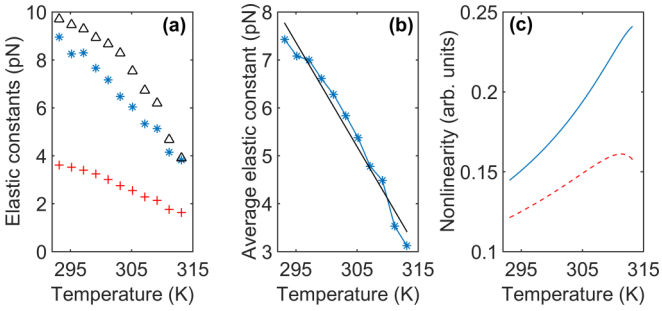

FIG. 11. (a) Measured elastic constants K_1 (blue stars), K_2 (red crosses), and K_3 (black triangles) versus temperature. (b) Average elastic constant $K_{\rm av}$ versus temperature (blue symbols) computed from the data shown in panel (a); the black solid line is the corresponding linear interpolation. (c) Behavior of the reorientational nonlinearity $\epsilon_0\epsilon_a/(4K_{\rm av})$ versus temperature for $\lambda = 1064$ nm (red dashed line) and 532 nm (blue solid line).

For small optical reorientations the term proportional to $(\partial\theta/\partial y)^2$ can be neglected. Thus, for an initial angle $\theta_0 = \pi/4$ an effective elastic constant equal to the average of the three elastic constants can be assumed. The elastic constants for 6CHBT are plotted in Fig. 11(a), as measured by all-optical methods [72]. All three elastic constants decrease monotonically versus temperature. Figure 11(b) shows the average Frank's constant $K_{\rm av} = (K_1 + K_2 + K_3)/3$: For temperatures not too close to the transition $T_{\rm NI}$, $K_{\rm av}$ can be satisfactorily approximated by a linear polynomial with coefficients $K_{\rm av} = -0.2173T + 71.4828$. Finally, Fig. 11(c) graphs the ratio of the optical anisotropy and the average elastic constant. All-optical reorientation is stronger at shorter wavelengths and increases with temperature up to $T = 40\,^{\circ}$C.

3. Width of solitons supported by a single nonlinearity

In the highly nonlocal approximation, fundamental solitons feature a Gaussian profile with waist determined by $[4/(n_0k_0^2|\phi_2|)]^{1/4}$, where n_0 is the unperturbed refractive index and k_0 the vacuum wave number. From Eq. (10), the existence curve of a soliton in the perturbative regime and due to a reorientational nonlinearity alone is

$$w_\theta^{\rm sol}(P) = \frac{1}{k_0}\sqrt{\frac{8\eta\pi K\cos^2\delta_0}{Z_0\epsilon_0\epsilon_a\sin[2(\theta_0-\delta_0)]\,\frac{dn_e}{d\theta}\big|_{\theta_0}}}\,\frac{1}{\sqrt{P}}, \qquad \text{(A3)}$$

whereas the thermal self-focusing provides an ordinary-wave soliton with

$$w_T^{\rm sol}(P) = \frac{1}{k_0}\sqrt{\frac{4\eta\pi\kappa}{n_\perp\alpha_{\rm ord}\frac{dn_\perp}{dT}}}\,\frac{1}{\sqrt{P}}. \qquad \text{(A4)}$$

The soliton width versus power as predicted by Eqs. (A3) and (A4) is plotted in Fig. 12 for a fixed sample temperature. The interaction between the two nonlinearities is neglected, considering only the reorientational effect for the extraordinary wave, and the thermal effect for the ordinary wave. For the infrared beam, corresponding to $\alpha \approx 10^2$ m^{-1}, the reorientational soliton is much narrower than the thermal one; the extraordinary self-trapped wave widens as the temperature approaches the transition value $T_{\rm NI}$. The size of the ordinary-wave thermal soliton is comparable with the extraordinary-wave soliton (i.e., a few microns) when the sample is close to the nematic-isotropic transition. For the green component, due to the large absorption, the roles are inverted. Green ordinary solitons can theoretically reach subwavelength size due to the large absorption, and this effect becomes more marked as the temperature approaches the nematic-to-isotropic transition $T_{\rm NI}$. In actual samples these waves are ruled out by the large losses associated with α and by the fact that strong absorption destroys the nematic phase.

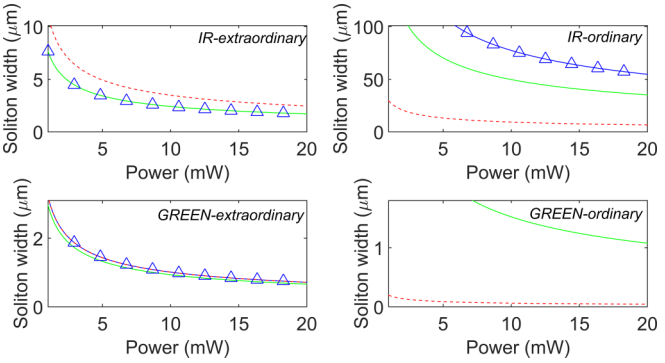

FIG. 12. Soliton existence curves in the plane width-power for extraordinary (left, reorientational nonlinearity) and ordinary (right, thermal nonlinearity) waves, as predicted by Eqs. (A3) and (A4). The first and second rows correspond to 6CHBT doped with Sudan Blue for $\lambda = 1064$ nm and 532 nm, respectively, with $\theta_0 = \pi/4$. Blue lines with triangles, green solid lines, and dashed red lines correspond to sample temperatures of $T_m = 295$ K, 305 K, and 315 K, respectively. The ordinary-wave green soliton at $T = 295$ K does not exist because at low temperatures as the thermal response is defocusing, according to Fig. 10.

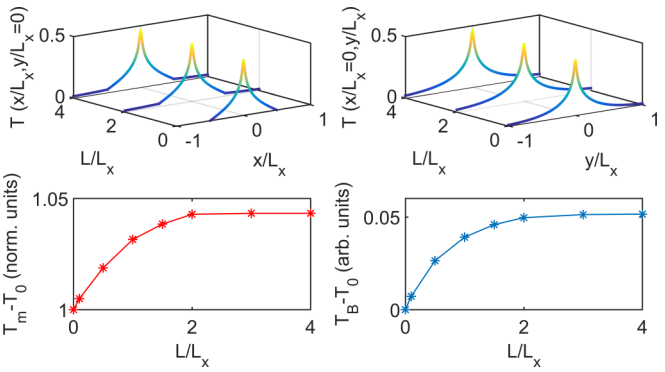

FIG. 13. Cross section on the cell midplanes of the temperature distribution versus x/L_x (a) and versus y/L_x (b) for three different thicknesses L/L_x of the glass interface. Maximum temperature change $T_m - T_0$ (normalized with respect to the value computed for $L = 0$ μm) (c) and temperature difference between the glass-NLC interface and the environment $T_B - T_0$ (d) versus glass thickness L/L_x (each point corresponds to a numerical simulation). The optical excitation is a Gaussian beam of waist $w/Lx = 0.02$. Here we assumed $\kappa_{\rm glass} = 10\kappa$.

4. Role of glass interfaces in the heat dissipation

In the main text, for the thermal problem we supposed that the temperature at the interface NLC-glass is equal to the environment temperature T_0, i.e., we set the conditions $T(x = L_x/2, y) = T(x = -L_x/2, y) = T_0$. The assumption corresponds to consider an infinite thermal conductivity for the glass. In real samples, the conductivity of the glass is 5–10 times larger than the NLC conductivity [38]. However, the actual thermal resistance of the glass depends strongly on the glass thickness and the punctual distribution of temperature. In the highly nonlocal limit, we expect that the heat flux is maximum away from the interfaces, and thus the approximation should be quite accurate. To estimate the accuracy of our approximation, we focus on the point $y = 0$, where the heat flux between glass and NLC is maximum for symmetry reasons. Setting $T_B = T(x = L_x/2, y = 0)$ and supposing a linear behavior for the temperature in the glass, the boundary condition at the interface reads $T_B - T_0 = L\frac{\kappa}{\kappa_{\text{glass}}}\frac{\partial T}{\partial x}|_{\text{NLC}}$, where L and κ_{glass} are the thickness and thermal conductivity of the glass, respectively. We define the effective thermal length of the NLC layer as $l_{\text{eff}}(w) \equiv (T_m - T_B)/\frac{\partial T}{\partial x}|_{\text{NLC}}$. The boundary condition now reads $\frac{T_B - T_0}{T_m - T_B} = \frac{L}{l_{\text{eff}}}\frac{\kappa}{\kappa_{\text{glass}}}$. Thus, the condition $T_B \approx T_0$ corresponds to $\frac{l_{\text{eff}}}{\kappa} \gg \frac{L}{\kappa_{\text{glass}}}$. Using Eq. (9) and results from Ref. [62], in the highly nonlocal limit we find

$$\frac{l_{\text{eff}}(w)}{L_x} \approx \frac{1}{\pi}\frac{\sum_{l=0}^{\infty}\frac{1}{2l+1}\,\text{erfc}\left[\frac{\pi(2l+1)w}{2\sqrt{2}L_x}\right]}{\sum_{l=0}^{\infty}(-1)^l\,\text{erfc}\left[\frac{\pi(2l+1)w}{2\sqrt{2}L_x}\right]}. \tag{A5}$$

Equation (A5) provides $l_{\text{eff}}/L_x \approx 1.35$ for $w/L_x = 0.02$. Temperature distribution in the sample for different normalized glass thickeness L/L_x is plotted in Figs. 13(a) and 13(b). We considered a Gaussian beam of normalized waist $w/L_x = 0.02$ and, due to the linearity of the Poisson equation, arbitrary amplitude. Moreover, we assumed $\kappa_{\text{glass}} = 10\kappa$, in agreement with typical NLC samples [38]. Temperature distribution undergoes a vertical shift as L is changed, whereas the shape in the NLC region stays almost unvaried. Figure 13(c) shows that the maximum of the optically induced perturbation $T_m - T_0$ increases monotonically, saturating when $L/L_x > 2$. Equation (A5) holds valid up to $L/L_x \approx 0.7$, that is, until the growth of $T_m - T_0$ is linear. In Fig. 13(d) the behavior of T_B is plotted. In agreement with Eq. (A5), at $L/L_x = 0.1$ the temperature of the glass-NLC interface is about 0.7% times higher than for $L/L_x = 0$. Real samples correspond usually to $L/L_x > 2$, where the variation in the maximum temperature change is already saturated and equal approximately to 5%.

[1] Young-Ki Kim, Bohdan Senyuk, and Oleg D. Lavrentovich, Molecular reorientation of a nematic liquid crystal by thermal expansion, Nat. Commun. **3**, 1133 (2012).

[2] P. G. DeGennes and J. Prost, *The Physics of Liquid Crystals* (Oxford Science, New York, 1993).

[3] Ming-Shan Tsai, I-Min Jiang, Chi-Yen Huang, and Chia-Chi Shih, Reorientational optical nonlinearity of nematic liquid-crystal cells near the nematic isotropic phase transition temperature, Opt. Lett. **28**, 2357 (2003).

[4] Shin-Tson Wu and Deng-Ke Yang, *Fundamentals of Liquid Crystal Devices* (Wiley, New York, 2006).

[5] B. Maune, R. Lawson, C. Gunn, A. Scherer, and L. Dalton, Electrically tunable ring resonators incorporating nematic liquid crystals as cladding layers, Appl. Phys. Lett. **83**, 4689 (2003).

[6] M. F. Moreira, I. C. S. Carvalho, W. Cao, C. Bailey, B. Taheri, and P. Palffy-Muhoray, Cholesteric liquid-crystals laser as an optic fiber-based temperature sensor, App. Phys. Lett. **85**, 2691 (2004).

[7] H. Coles and S. Morris, Liquid-crystal lasers, Nat. Photon. **4**, 676 (2010).

[8] Z. Zhang, Z. You, and D. Chu, Fundamentals of phase-only liquid crystal on silicon (lcos) devices, Light: Sci. Appl. **3**, e213 (2014).

[9] L. Marrucci, C. Manzo, and D. Paparo, Pancharatnam-Berry phase optical elements for wave front shaping in the visible domain: Switchable helical mode generation, Appl. Phys. Lett. **88**, 221102 (2006).

[10] N.V. Tabiryan and B.Y. Zeldovich, The orientational optical nonlinearity of liquid-crystals, Mol. Cryst. Liq. Cryst. **62**, 237 (1980).

[11] I. C. Khoo, *Liquid Crystals: Physical Properties and Nonlinear Optical Phenomena* (Wiley, New York, 1995).

[12] George K. L. Wong and Y. R. Shen, Optical-Field-Induced Ordering in the Isotropic Phase of a Nematic Liquid Crystal, Phys. Rev. Lett. **30**, 895 (1973).

[13] S. D. Durbin, S. M. Arakelian, and Y. R. Shen, Optical-Field-Induced Birefringence and Freedericksz Transition in a Nematic Liquid Crystal, Phys. Rev. Lett. **47**, 1411 (1981).

[14] M. Peccianti, A. Pasquazi, G. Assanto, and R. Morandotti, Enhancement of third-harmonic generation in nonlocal spatial solitons, Opt. Lett. **35**, 3342 (2010).

[15] A. Piccardi, A. Alberucci, N. Tabiryan, and G. Assanto, Dark nematicons, Opt. Lett. **36**, 1356 (2011).

[16] M. Warenghem, J. F. Blach, and J. F. Henninot, Thermonematicon: an unnatural coexistence of solitons in liquid crystals?, J. Opt. Soc. Am. B **25**, 1882 (2008).

[17] Ian B. Burgess, Marco Peccianti, Gaetano Assanto, and Roberto Morandotti, Accessible Light Bullets via Synergetic Nonlinearities, Phys. Rev. Lett. **102**, 203903 (2009).

[18] Urszula A. Laudyn, Michał Kwasny, Armando Piccardi, Mirosław A. Karpierz, Roman Dabrowski, Olga Chojnowska, Alessandro Alberucci, and Gaetano Assanto, Nonlinear competition in nematicon propagation, Opt. Lett. **40**, 5235 (2015).

[19] I. Jánossy and T. Kósa, Influence of anthraquinone dyes on optical reorientation of nematic liquid crystals, Opt. Lett. **17**, 1183 (1992).

[20] R. Muenster, M. Jarasch, X. Zhuang, and Y. R. Shen, Dye-Induced Enhancement of Optical Nonlinearity in Liquids and Liquid Crystals, Phys. Rev. Lett. **78**, 42 (1997).

[21] S. Ferjani, V. Barna, A. De Luca, C. Versace, N. Scaramuzza, R. Bartolino, and G. Strangi, Thermal behavior of random lasing in dye-doped nematic liquid crystals, Appl. Phys. Lett. **89**, 121109 (2006).

[22] Monika A. M. Marte, Competing nonlinearities, Phys. Rev. A **49**, R3166 (1994).
[23] F. Maucher, T. Pohl, S. Skupin, and W. Krolikowski, Self-Organization of Light in Optical Media with Competing Nonlinearities, Phys. Rev. Lett. **116**, 163902 (2016).
[24] B. L. Lawrence, M. Cha, J.U. Kang, G. Stegeman, G. Baker, J. Meth, and S. Etemad, Large purely refractive nonlinear index of single crystal P-toluene sulphonate (PTS) at 1600 nm, Electron. Lett. **30**, 447 (1994).
[25] Ewan M. Wright, Brian L. Lawrence, William Torruellas, and George Stegeman, Stable self-trapping and ring formation in polydiacetylene para-toluene sulfonate, Opt. Lett. **20**, 2481 (1995).
[26] Bonggu Shim, Samuel E. Schrauth, Alexander L. Gaeta, Moran Klein, and Gadi Fibich, Loss of Phase of Collapsing Beams, Phys. Rev. Lett. **108**, 043902 (2012).
[27] Alexander V. Buryak, Stefano Trillo, and Yuri S. Kivshar, Optical solitons supported by competing nonlinearities, Opt. Lett. **20**, 1961 (1995).
[28] M. Quiroga-Teixeiro and H. Michinel, Stable azimuthal stationary state in quintic nonlinear optical media, J. Opt. Soc. Am. B **14**, 2004 (1997).
[29] D. Mihalache, D. Mazilu, F. Lederer, L.-C. Crasovan, Y. V. Kartashov, L. Torner, and B. A. Malomed, Stable solitons of even and odd parities supported by competing nonlocal nonlinearities, Phys. Rev. E **74**, 066614 (2006).
[30] Edilson L. Falcão-Filho, Cid B. de Araújo, Georges Boudebs, Hervé Leblond, and Vladimir Skarka, Robust Two-Dimensional Spatial Solitons in Liquid Carbon Disulfide, Phys. Rev. Lett. **110**, 013901 (2013).
[31] Yaron Silberberg, Collapse of optical pulses, Opt. Lett. **15**, 1282 (1990).
[32] D. Mihalache, D. Mazilu, B. A. Malomed, F. Lederer, L.-C. Crasovan, Y. V. Kartashov, and L. Torner, Stable three-dimensional optical solitons supported by competing quadratic and self-focusing cubic nonlinearities, Phys. Rev. E **74**, 047601 (2006).
[33] Erez Braun, Luc P. Faucheux, and Albert Libchaber, Strong self-focusing in nematic liquid crystals, Phys. Rev. A **48**, 611 (1993).
[34] A. W. Snyder and D. J. Mitchell, Accessible solitons, Science **276**, 1538 (1997).
[35] C. Conti, M. Peccianti, and G. Assanto, Route to Nonlocality and Observation of Accessible Solitons, Phys. Rev. Lett. **91**, 073901 (2003).
[36] C. Rotschild, O. Cohen, O. Manela, M. Segev, and T. Carmon, Solitons in Nonlinear Media with an Infinite Range of Nonlocality: First Observation of Coherent Elliptic Solitons and of Vortex-Ring Solitons, Phys. Rev. Lett. **95**, 213904 (2005).
[37] M. Warenghem, J. F. Blach, and J. F. Henninot, Measuring and monitoring optically induced thermal or orientational nonlocality in nematic liquid crystal, Mol. Cryst. Liq. Cryst. **454**, 297/[699] (2006).
[38] F. Simoni, *Nonlinear Optical Properties of Liquid Crystals* (World Scientific, Singapore, 1997).
[39] Jun Li and Shin-Tson Wu, Extended cauchy equations for the refractive indices of liquid crystals, J. Appl. Phys. **95**, 896 (2004).
[40] F. Derrien, J. F. Henninot, M. Warenghem, and G. Abbate, A thermal (2d+1) spatial optical soliton in a dye doped liquid crystal, J. Opt. A: Pure Appl. Opt. **2**, 332 (2000).
[41] X. Hutsebaut, C. Cambournac, M. Haelterman, A. Adamski, and K. Neyts, Single-component higher-order mode solitons in liquid crystals, Opt. Commun. **233**, 211 (2004).
[42] A. Alberucci, A. Piccardi, M. Peccianti, M. Kaczmarek, and G. Assanto, Propagation of spatial optical solitons in a dielectric with adjustable nonlinearity, Phys. Rev. A **82**, 023806 (2010).
[43] M. Warenghem, J. F. Henninot, and G. Abbate, Non linearly induced self waveguiding structure in dye doped nematic liquid crystals confined in capillaries, Opt. Express **2**, 483 (1998).
[44] S. D. Durbin, S. M. Arakelian, M. M. Cheung, and Y. R. Shen, Highly nonlinear optical effects in liquid crystals, J. Phys. Colloques **44**, C2-161 (1983).
[45] B. Ya. Zel'dovich, N. F. Pilipetskii, A. V. Sukhov, and N. V. Tabiryan, Giant optical nonlinearity in the mesophase of a nematic liquid crystals (NCL), JETP Lett. **31**, 263 (1980).
[46] M. Peccianti and G. Assanto, Nematicons, Phys. Rep. **516**, 147 (2012).
[47] M. Peccianti, C. Conti, G. Assanto, A. De Luca, and C. Umeton, Routing of anisotropic spatial solitons and modulational instability in nematic liquid crystals, Nature **432**, 733 (2004).
[48] J Beeckman, K Neyts, and M Haelterman, Patterned electrode steering of nematicons, J. Optics A: Pure Appl. Opt. **8**, 214 (2006).
[49] A. Piccardi, G. Assanto, L. Lucchetti, and F. Simoni, All-optical steering of soliton waveguides in dye-doped liquid crystals, Appl. Phys. Lett. **93**, 171104 (2008).
[50] Yana V. Izdebskaya, Vladlen G. Shvedov, Anton S. Desyatnikov, Wieslaw Krolikowski, and Yuri S. Kivshar, Soliton bending and routing induced by interaction with curved surfaces in nematic liquid crystals, Opt. Lett. **35**, 1692 (2010).
[51] G. Assanto, *Nematicons: Spatial Optical Solitons in Nematic Liquid Crystals* (Wiley, New York, 2012).
[52] Urszula A. Laudyn and Miroslaw A. Karpierz, Nematicons deflection through interaction with disclination lines in chiral nematic liquid crystals, Appl. Phys. Lett. **103**, 221104 (2013).
[53] A. Piccardi, A. Alberucci, N. Kravets, O. Buchnev, and G. Assanto, Power-controlled transition from standard to negative refraction in reorientational soft matter, Nat. Commun. **5**, 5533 (2014).
[54] Yana V. Izdebskaya, Routing of spatial solitons by interaction with rod microelectrodes, Opt. Lett. **39**, 1681 (2014).
[55] Y. Izdebskaya, V. Shvedov, G. Assanto, and W. Krolikowski, Magnetic routing of light-induced waveguides, Nat. Comm. **8**, 14452 (2017).
[56] O. Bang, W. Krolikowski, J. Wyller, and J. J. Rasmussen, Collapse arrest and soliton stabilization in nonlocal nonlinear media, Phys. Rev. E **66**, 046619 (2002).
[57] C. Conti, M. Peccianti, and G. Assanto, Observation of Optical Spatial Solitons in a Highly Nonlocal Medium, Phys. Rev. Lett. **92**, 113902 (2004).
[58] Alessandro Alberucci, Chandroth P. Jisha, Noel F. Smyth, and Gaetano Assanto, Spatial optical solitons in highly nonlocal media, Phys. Rev. A **91**, 013841 (2015).
[59] A. Alberucci, C. P. Jisha, and G. Assanto, Breather solitons in highly nonlocal media, J. Opt. **18**, 125501 (2016).

[60] K. Milanchian, E. Abdi, H. Tajalli, S. Ahmadi K., and M.S. Zakerhamidi, Nonlinear refractive index of some anthraquinone dyes in 1294-1b liquid crystal, Opt. Commun. **285**, 761 (2012).

[61] J. Beeckman, K. Neyts, X. Hutsebaut, C. Cambournac, and M. Haelterman, Time dependence of soliton formation in planar cells of nematic liquid crystals, IEEE J. Quantum Electron. **41**, 735 (2005).

[62] A. Alberucci and G. Assanto, Propagation of optical spatial solitons in finite-size media: interplay between nonlocality and boundary conditions, J. Opt. Soc. Am. B **24**, 2314 (2007).

[63] In actual cases this is valid, at least to first approximation: the temperature is assumed equal to T_0 at the edges of the sample, whereas the optical reorientation ψ vanishes at the interfaces under strong anchoring conditions.

[64] S. Ouyang, Q. Guo, and W. Hu, Perturbative analysis of generally nonlocal spatial optical solitons, Phys. Rev. E **74**, 036622 (2006).

[65] A. Alberucci, C. P. Jisha, and G. Assanto, Accessible solitons in diffusive media, Opt. Lett. **39**, 4317 (2014).

[66] N. Kravets, A. Piccardi, A. Alberucci, O. Buchnev, M. Kaczmarek, and G. Assanto, Bistability with Optical Beams Propagating in a Reorientational Medium, Phys. Rev. Lett. **113**, 023901 (2014).

[67] E. Santamato, G. Abbate, P. Maddalena, and Y. R. Shen, Optically induced twist Fréedericksz transitions in planar aligned nematic liquid crystals, Phys. Rev. A **36**, 2389 (1987).

[68] A. Alberucci, A. Piccardi, N. Kravets, and G. Assanto, Beam hysteresis via reorientational self-focusing, Opt. Lett. **39**, 5830 (2014).

[69] In general, optical reorientation also modulates the thermal properties. We neglect this correction consistently with the background orientation $\theta_0 = \pi/4$, as ψ remains small with respect to θ_0.

[70] N. Karimi, A. Alberucci, O. Buchnev, M. Virkki, M. Kauranen, and G. Assanto, Phase-front curvature effects on nematicon generation, J. Opt. Soc. Am. B **33**, 903 (2016).

[71] Pawel S. Jung, Wieslaw Krolikowski, Urszula A. Laudyn, Marek Trippenbach, and Miroslaw A. Karpierz, Supermode spatial optical solitons in liquid crystals with competing nonlinearities, Phys. Rev. A **95**, 023820 (2017).

[72] B. Klus, U. A. Laudyn, M. A. Karpierz, and B. Sahraoui, All-optical measurement of elastic constants in nematic liquid crystals, Opt. Express **22**, 30257 (2014).